Electronic supporting information: Impact of crystal structure on the lattice thermal conductivity of the IV-VI chalcogenides

Sophie K. Guillemot, Ady Suwardi, Nikolas Kaltsoyannis, and Jonathan M. Skelton

1 Phonon dispersion and density of states curves

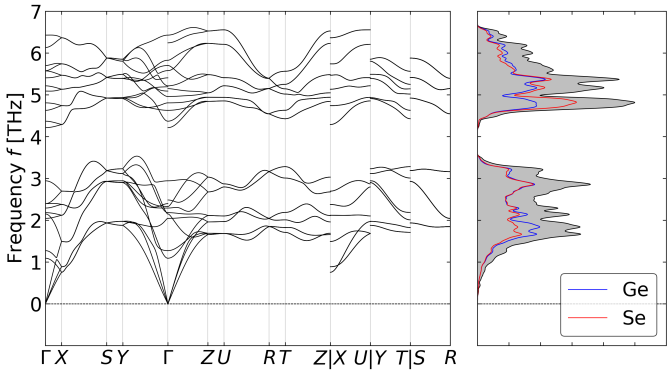

Fig. S1 Phonon dispersion and density of states (DoS) curves for *Pnma* GeSe. The total DoS is shown as a shaded grey curve and the projections onto the Ge and Se atoms are shown as blue and red lines respectively.

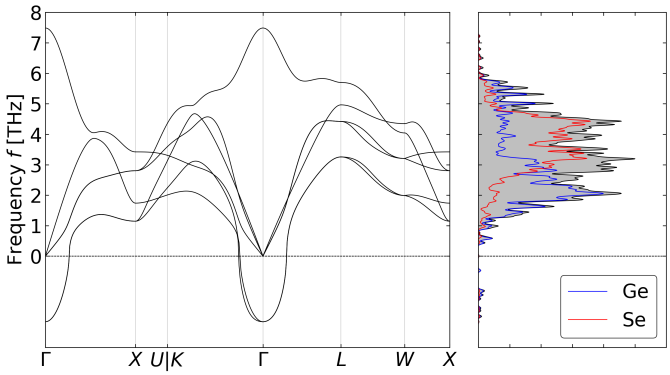

Fig. S2 Phonon dispersion and density of states (DoS) curves for $Fm\bar{3}m$ GeSe. The total DoS is shown as a shaded grey curve and the projections onto the Ge and Se atoms are shown as blue and red lines respectively.

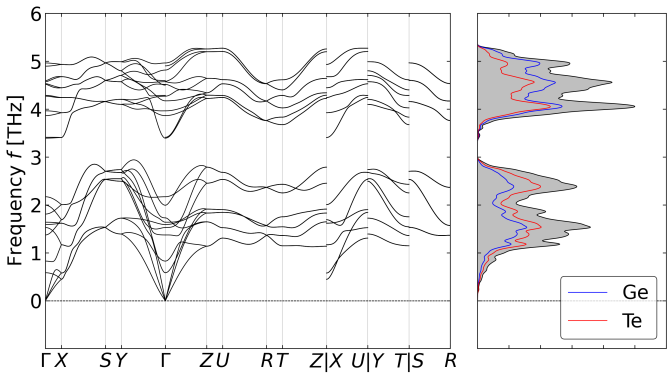

Fig. S3 Phonon dispersion and density of states (DoS) curves for *Pnma* GeTe. The total DoS is shown as a shaded grey curve and the projections onto the Ge and Te atoms are shown as blue and red lines respectively.

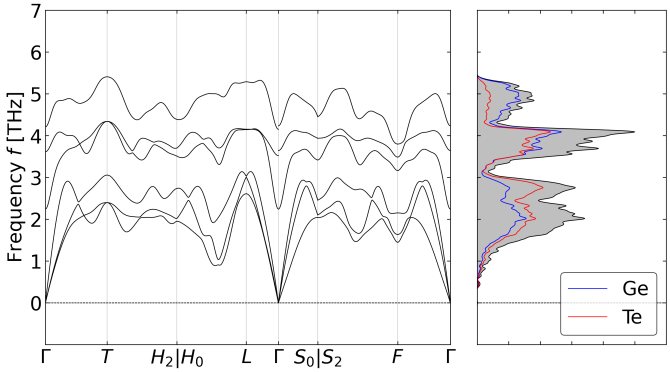

Fig. S4 Phonon dispersion and density of states (DoS) curves for *R*3*m* GeTe. The total DoS is shown as a shaded grey curve and the projections onto the Ge and Te atoms are shown as blue and red lines respectively.

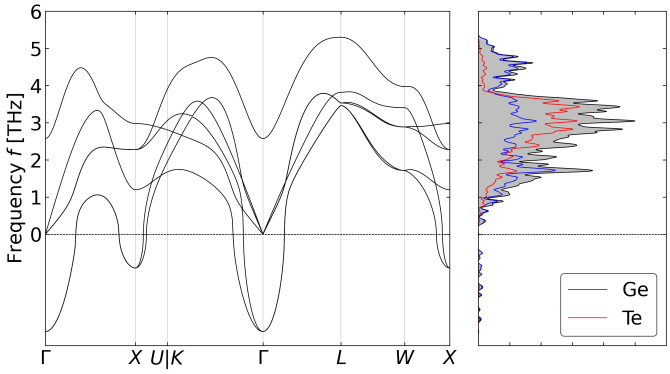

Fig. S5 Phonon dispersion and density of states (DoS) curves for $Fm\bar{3}m$ GeTe. The total DoS is shown as a shaded grey curve and the projections onto the Ge and Te atoms are shown as blue and red lines respectively.

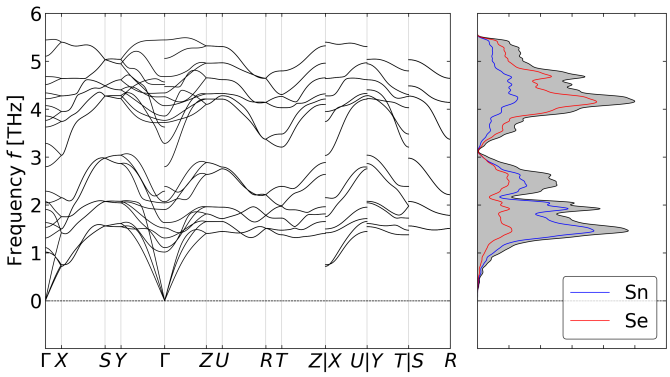

Fig. S6 Phonon dispersion and density of states (DoS) curves for *Pnma* SnSe. The total DoS is shown as a shaded grey curve and the projections onto the Sn and Se atoms are shown as blue and red lines respectively.

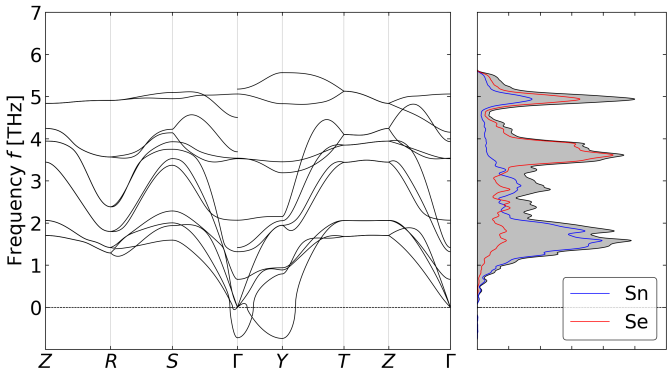

Fig. S7 Phonon dispersion and density of states (DoS) curves for *Cmcm* SnSe. The total DoS is shown as a shaded grey curve and the projections onto the Sn and Se atoms are shown as blue and red lines respectively.

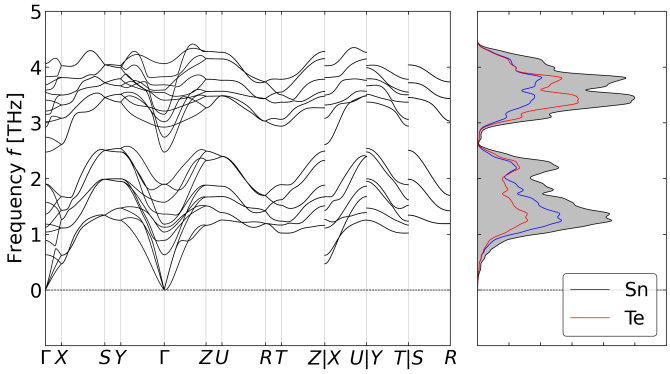

Fig. S8 Phonon dispersion and density of states (DoS) curves for *Pnma* SnTe. The total DoS is shown as a shaded grey curve and the projections onto the Sn and Te atoms are shown as blue and red lines respectively.

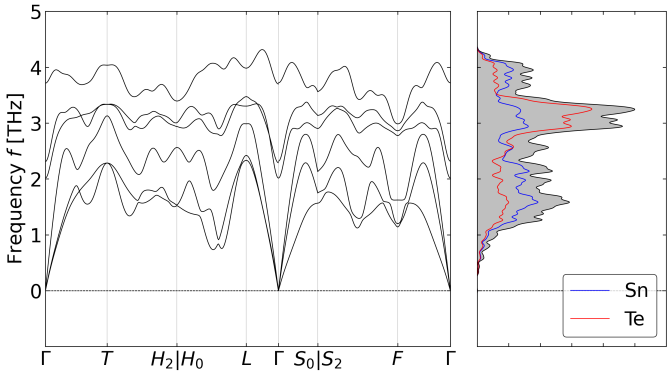

Fig. S9 Phonon dispersion and density of states (DoS) curves for $R3m$ SnTe. The total DoS is shown as a shaded grey curve and the projections onto the Sn and Te atoms are shown as blue and red lines respectively.

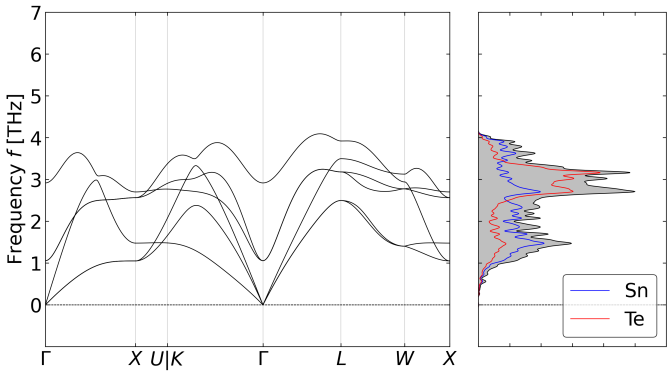

Fig. S10 Phonon dispersion and density of states (DoS) curves for $Fm\bar{3}m$ SnTe. The total DoS is shown as a shaded grey curve and the projections onto the Sn and Te atoms are shown as blue and red lines respectively.

2 Anisotropy in the lattice thermal conductivity

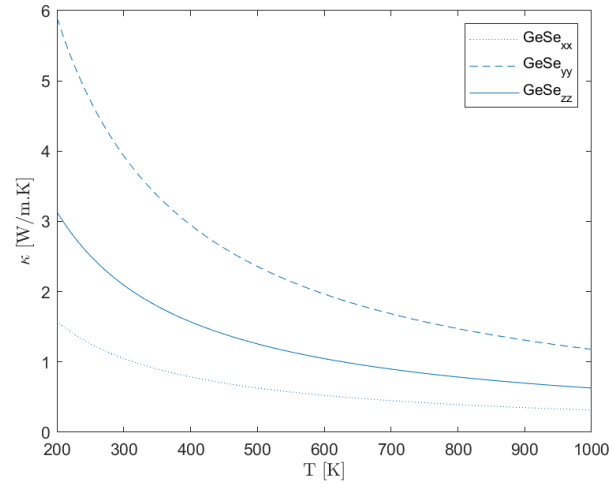

Fig. S11 Diagonal components of the calculated lattice thermal conductivity tensors, κ_{xx}, κ_{yy} and κ_{zz}, as a function of temperature for *Pnma* GeSe.

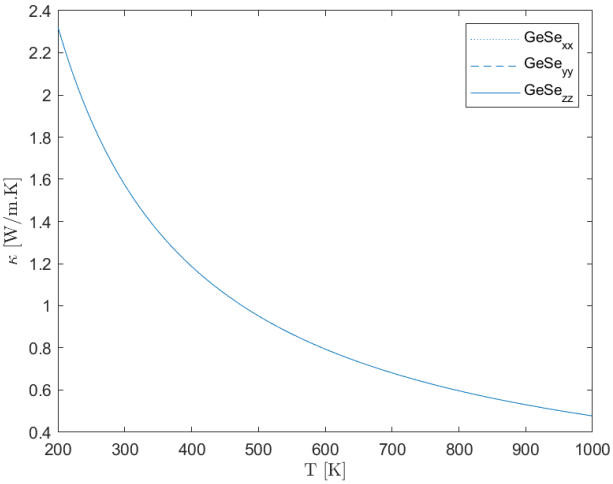

Fig. S12 Diagonal components of the calculated lattice thermal conductivity tensors, κ_{xx}, κ_{yy} and κ_{zz}, as a function of temperature for $Fm\bar{3}m$ GeSe.

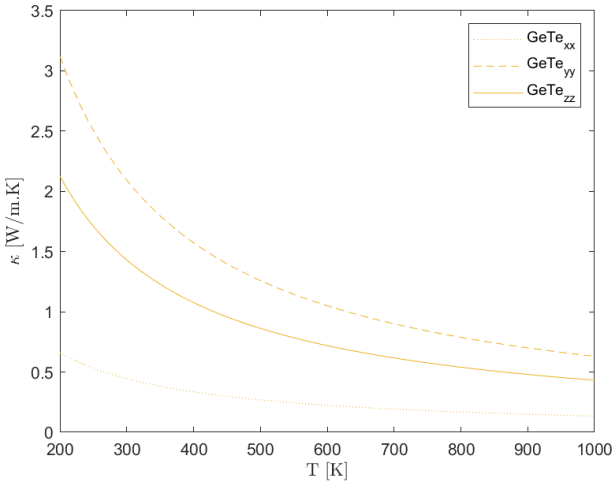

Fig. S13 Diagonal components of the calculated lattice thermal conductivity tensors, κ_{xx}, κ_{yy} and κ_{zz}, as a function of temperature for *Pnma* GeTe.

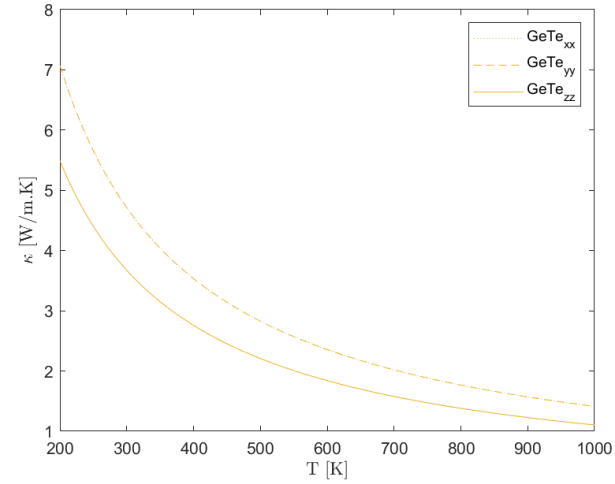

Fig. S14 Diagonal components of the calculated lattice thermal conductivity tensors, κ_{xx}, κ_{yy} and κ_{zz}, as a function of temperature for $R3m$ GeTe.

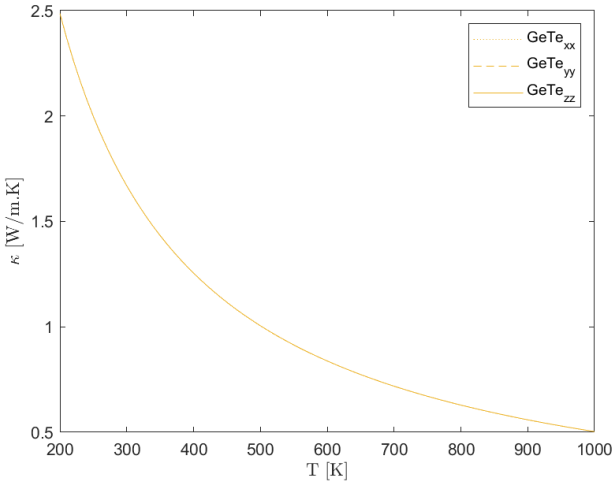

Fig. S15 Diagonal components of the calculated lattice thermal conductivity tensors, κ_{xx}, κ_{yy} and κ_{zz}, as a function of temperature for $Fm\bar{3}m$ GeTe.

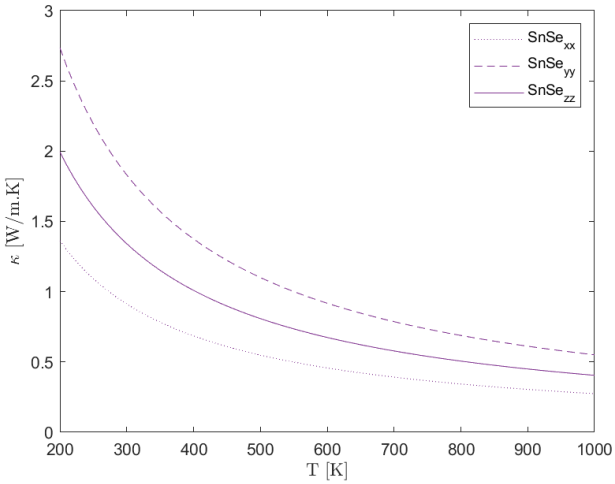

Fig. S16 Diagonal components of the calculated lattice thermal conductivity tensors, κ_{xx}, κ_{yy} and κ_{zz}, as a function of temperature for *Pnma* SnSe.

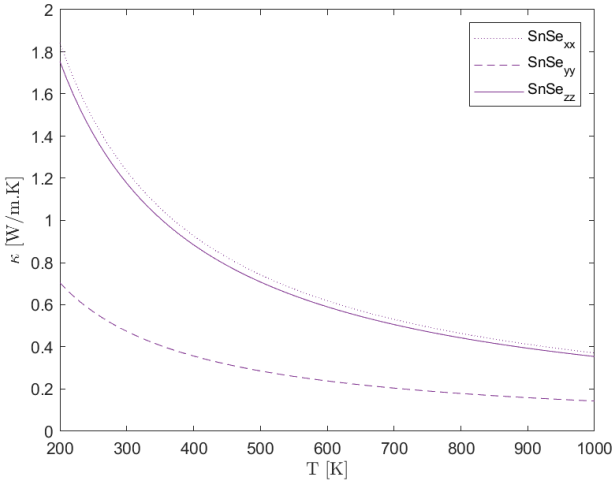

Fig. S17 Diagonal components of the calculated lattice thermal conductivity tensors, κ_{xx}, κ_{yy} and κ_{zz}, as a function of temperature for *Cmcm* SnSe.

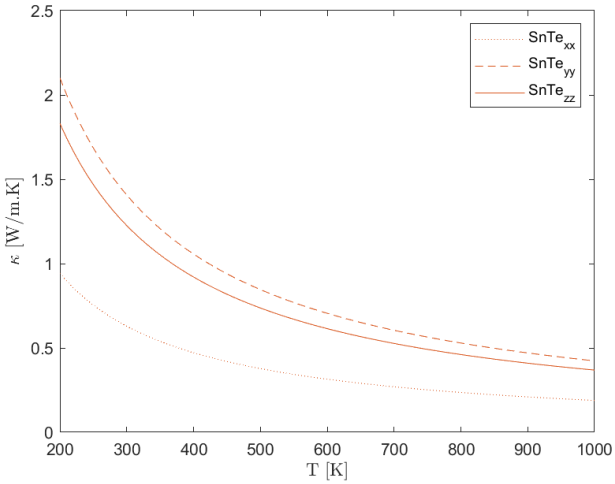

Fig. S18 Diagonal components of the calculated lattice thermal conductivity tensors, κ_{xx}, κ_{yy} and κ_{zz}, as a function of temperature for *Pnma* SnTe.

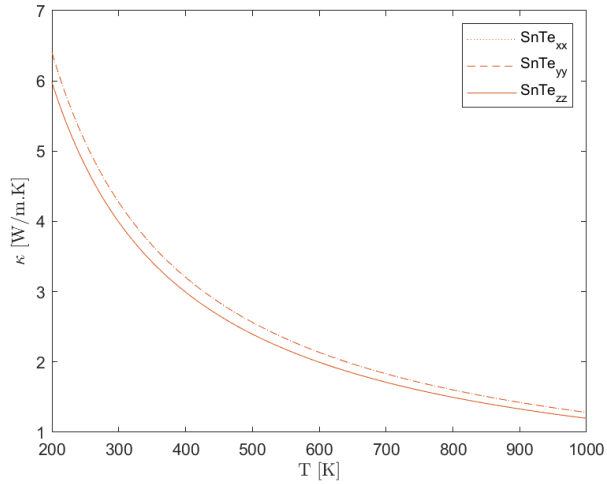

Fig. S19 Diagonal components of the calculated lattice thermal conductivity tensors, κ_{xx}, κ_{yy} and κ_{zz}, as a function of temperature for $R3m$ SnTe.

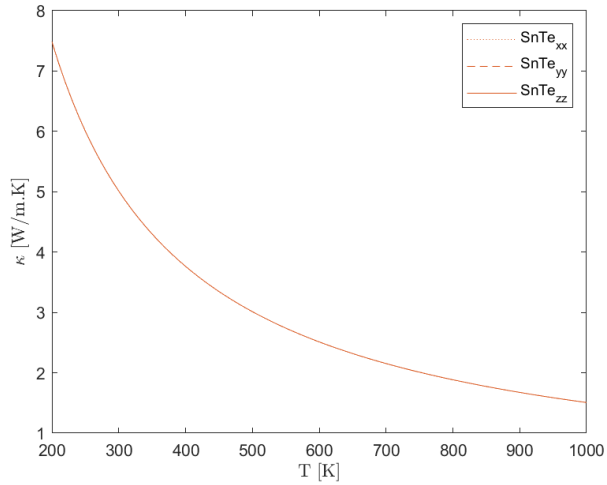

Fig. S20 Diagonal components of the calculated lattice thermal conductivity tensors, κ_{xx}, κ_{yy} and κ_{zz}, as a function of temperature for $Fm\bar{3}m$ SnTe.

3 Averaged phonon lifetimes

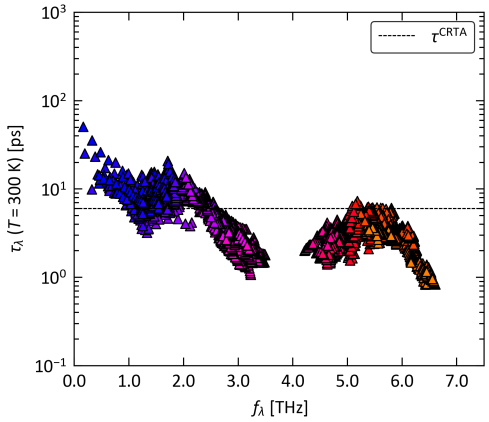

Fig. S21 Comparison of the averaged lifetime τ^{CRTA} for *Pnma* GeSe to the spectrum of phonon lifetimes at $T = 300$ K.

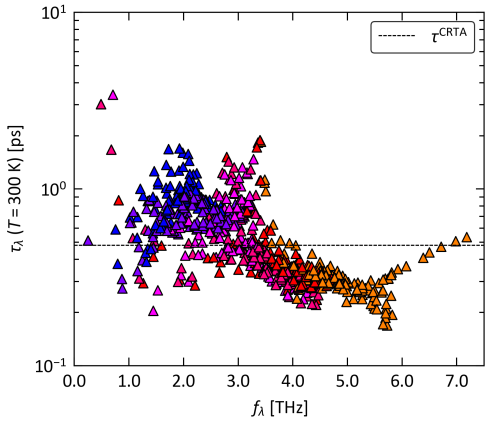

Fig. S22 Comparison of the averaged lifetime τ^{CRTA} for $Fm\bar{3}m$ GeSe to the spectrum of phonon lifetimes at $T = 300$ K.

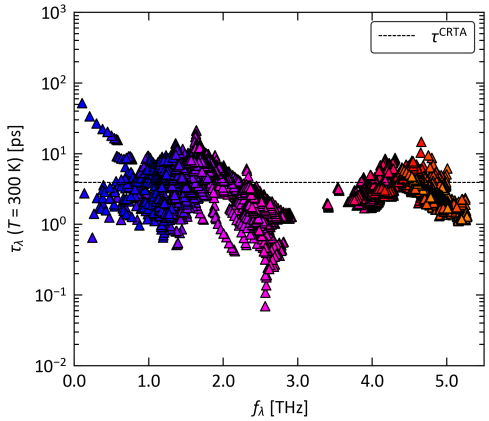

Fig. S23 Comparison of the averaged lifetime τ^{CRTA} for *Pnma* GeTe to the spectrum of phonon lifetimes at $T = 300$ K.

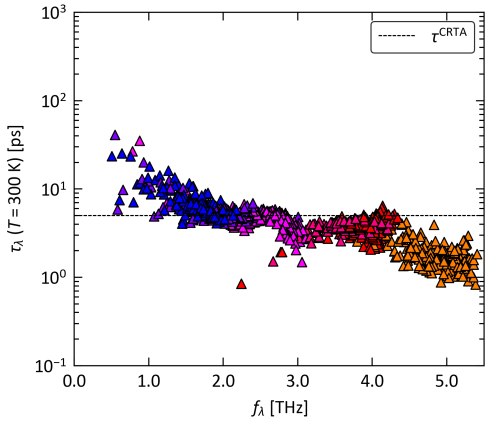

Fig. S24 Comparison of the averaged lifetime τ^{CRTA} for $R3m$ GeTe to the spectrum of phonon lifetimes at $T = 300$ K.

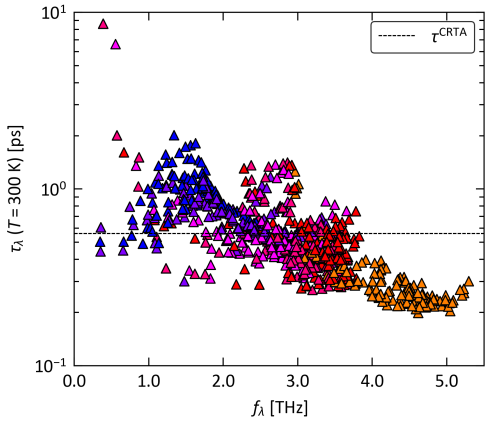

Fig. S25 Comparison of the averaged lifetime τ^{CRTA} for $Fm\bar{3}m$ GeTe to the spectrum of phonon lifetimes at $T = 300$ K.

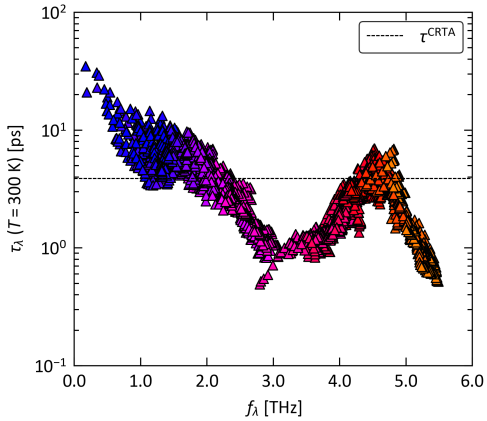

Fig. S26 Comparison of the averaged lifetime τ^{CRTA} for *Pnma* SnSe to the spectrum of phonon lifetimes at $T = 300$ K.

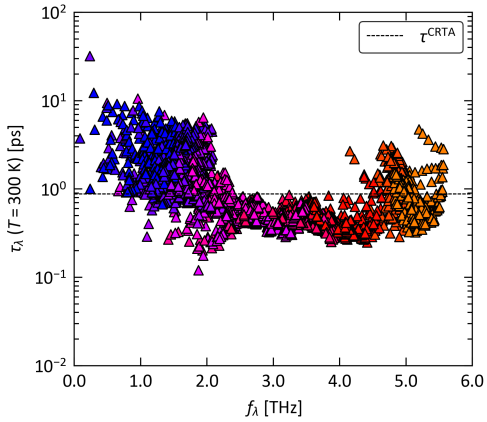

Fig. S27 Comparison of the averaged lifetime τ^{CRTA} for *Cmcm* SnSe to the spectrum of phonon lifetimes at $T = 300$ K.

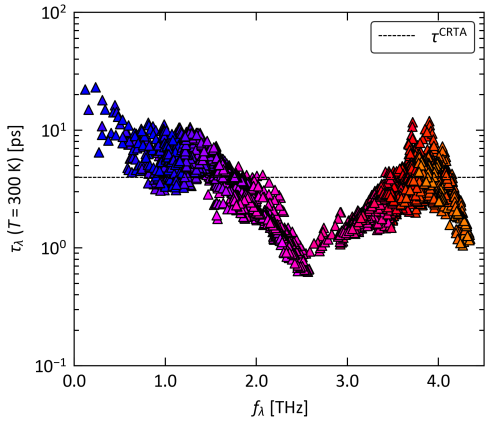

Fig. S28 Comparison of the averaged lifetime τ^{CRTA} for *Pnma* SnTe to the spectrum of phonon lifetimes at $T = 300$ K.

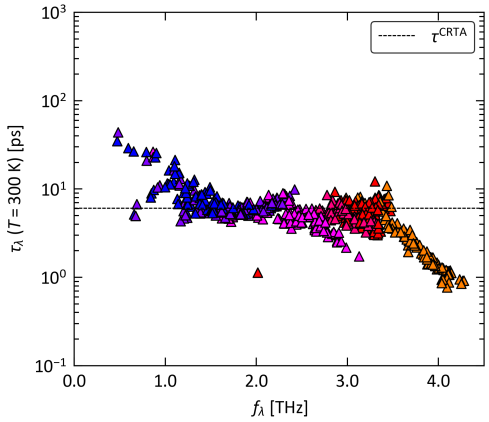

Fig. S29 Comparison of the averaged lifetime τ^{CRTA} for $R3m$ SnTe to the spectrum of phonon lifetimes at $T = 300$ K.

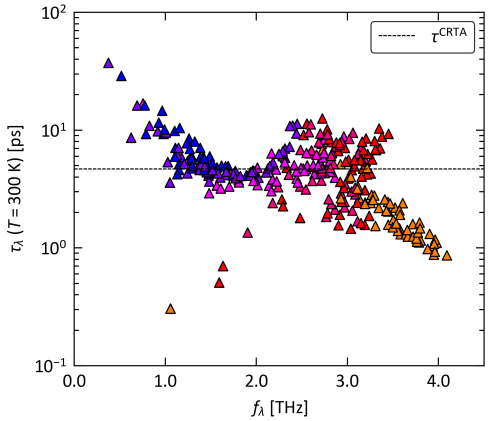

Fig. S30 Comparison of the averaged lifetime τ^{CRTA} for $Fm\bar{3}m$ SnTe to the spectrum of phonon lifetimes at $T = 300$ K.

4 Phonon-scattering phase space

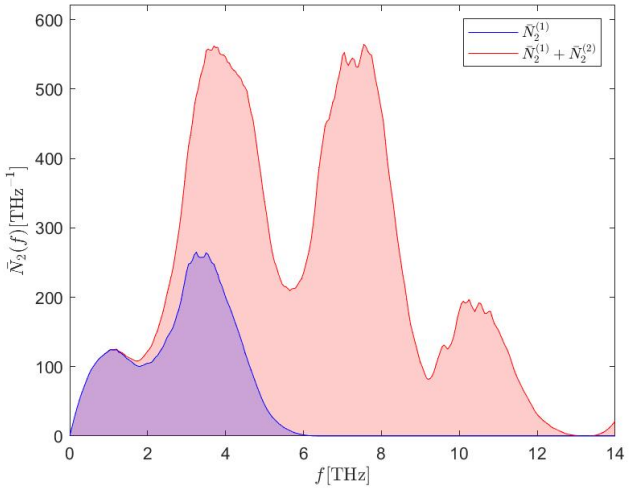

Fig. S31 Averaged two-phonon weighted joint density of states (w-JDoS) functions $\bar{N}_2(f)$ for *Pnma* GeSe at $T = 300$ K. The plot is drawn as a stacked area plot showing the contributions from collision ($\bar{N}_2^{(1)}$) and decay ($\bar{N}_2^{(2)}$) processes in blue and red, respectively (the red line shows the sum $\bar{N}_2^{(1)} + \bar{N}_2^{(2)}$).

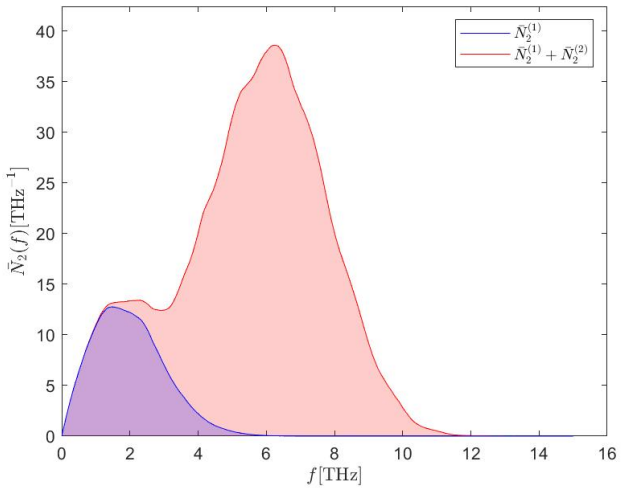

Fig. S32 Averaged two-phonon weighted joint density of states (w-JDoS) functions $\bar{N}_2(f)$ for $Fm\bar{3}m$ GeSe at $T = 300$ K. The plot is drawn as a stacked area plot showing the contributions from collision ($\bar{N}_2^{(1)}$) and decay ($\bar{N}_2^{(2)}$) processes in blue and red, respectively (the red line shows the sum $\bar{N}_2^{(1)} + \bar{N}_2^{(2)}$).

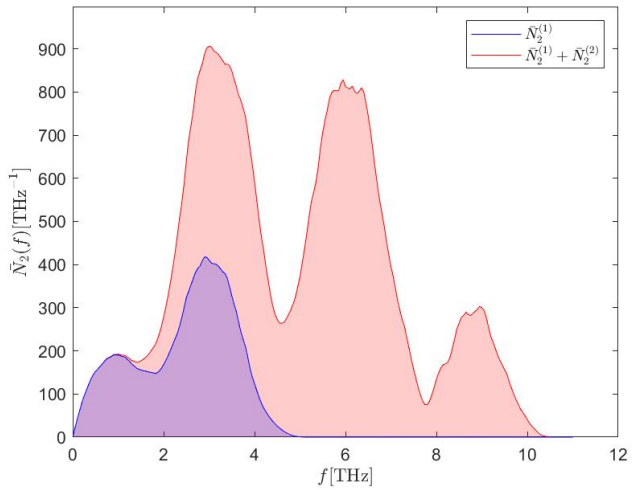

Fig. S33 Averaged two-phonon weighted joint density of states (w-JDoS) functions $\bar{N}_2(f)$ for *Pnma* GeTe at $T = 300$ K. The plot is drawn as a stacked area plot showing the contributions from collision ($\bar{N}_2^{(1)}$) and decay ($\bar{N}_2^{(2)}$) processes in blue and red, respectively (the red line shows the sum $\bar{N}_2^{(1)} + \bar{N}_2^{(2)}$).

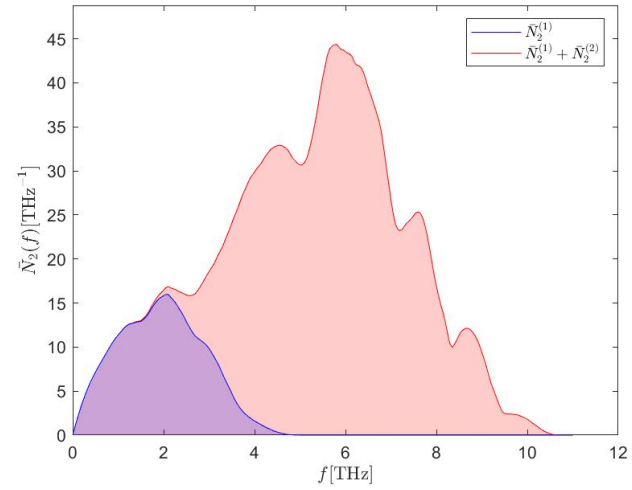

Fig. S34 Averaged two-phonon weighted joint density of states (w-JDoS) functions $\bar{N}_2(f)$ for $R3m$ GeTe at $T = 300$ K. The plot is drawn as a stacked area plot showing the contributions from collision ($\bar{N}_2^{(1)}$) and decay ($\bar{N}_2^{(2)}$) processes in blue and red, respectively (the red line shows the sum $\bar{N}_2^{(1)} + \bar{N}_2^{(2)}$).

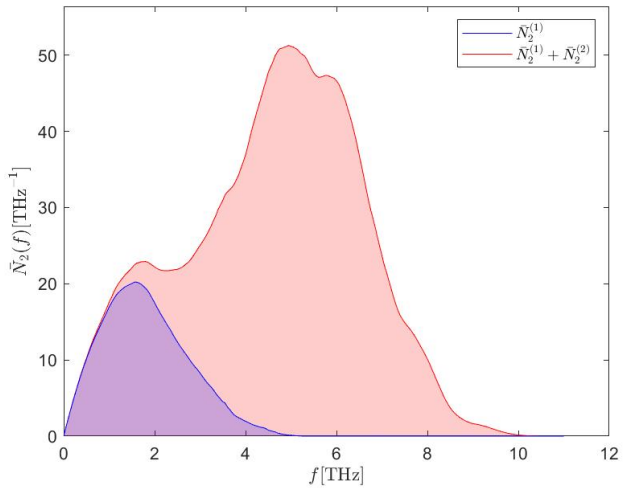

Fig. S35 Averaged two-phonon weighted joint density of states (w-JDoS) functions $\bar{N}_2(f)$ for $Fm\bar{3}m$ GeTe at $T = 300$ K. The plot is drawn as a stacked area plot showing the contributions from collision ($\bar{N}_2^{(1)}$) and decay ($\bar{N}_2^{(2)}$) processes in blue and red, respectively (the red line shows the sum $\bar{N}_2^{(1)} + \bar{N}_2^{(2)}$).

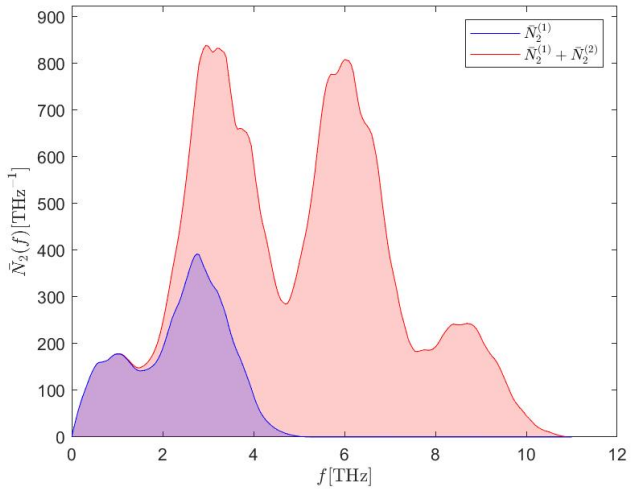

Fig. S36 Averaged two-phonon weighted joint density of states (w-JDoS) functions $\bar{N}_2(f)$ for *Pnma* SnSe at $T = 300$ K. The plot is drawn as a stacked area plot showing the contributions from collision ($\bar{N}_2^{(1)}$) and decay ($\bar{N}_2^{(2)}$) processes in blue and red, respectively (the red line shows the sum $\bar{N}_2^{(1)} + \bar{N}_2^{(2)}$).

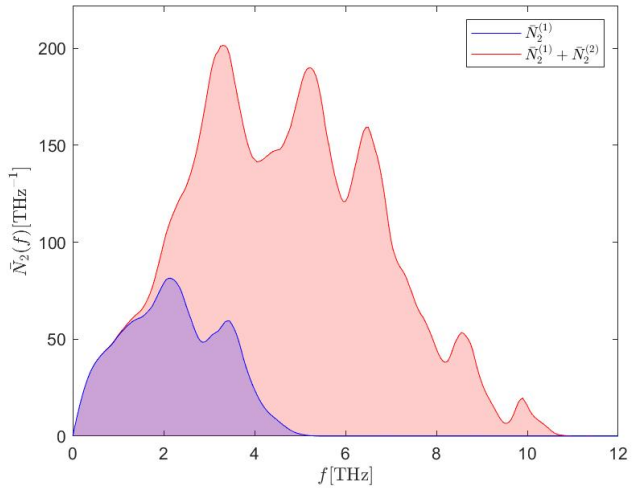

Fig. S37 Averaged two-phonon weighted joint density of states (w-JDoS) functions $\bar{N}_2(f)$ for *Cmcm* SnSe at $T = 300$ K. The plot is drawn as a stacked area plot showing the contributions from collision ($\bar{N}_2^{(1)}$) and decay ($\bar{N}_2^{(2)}$) processes in blue and red, respectively (the red line shows the sum $\bar{N}_2^{(1)} + \bar{N}_2^{(2)}$).

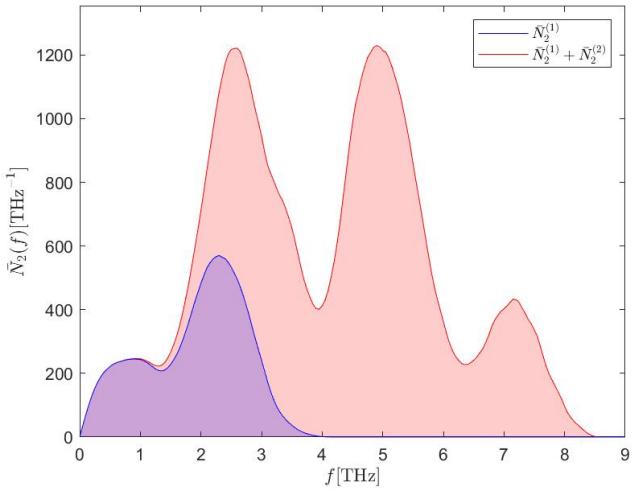

Fig. S38 Averaged two-phonon weighted joint density of states (w-JDoS) functions $\bar{N}_2(f)$ for *Pnma* SnTe at $T = 300$ K. The plot is drawn as a stacked area plot showing the contributions from collision ($\bar{N}_2^{(1)}$) and decay ($\bar{N}_2^{(2)}$) processes in blue and red, respectively (the red line shows the sum $\bar{N}_2^{(1)} + \bar{N}_2^{(2)}$).

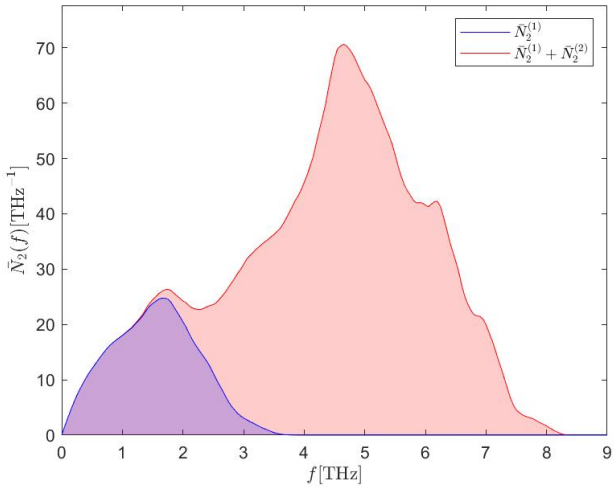

Fig. S39 Averaged two-phonon weighted joint density of states (w-JDoS) functions $\bar{N}_2(f)$ for $R3m$ SnTe at $T = 300$ K. The plot is drawn as a stacked area plot showing the contributions from collision ($\bar{N}_2^{(1)}$) and decay ($\bar{N}_2^{(2)}$) processes in blue and red, respectively (the red line shows the sum $\bar{N}_2^{(1)} + \bar{N}_2^{(2)}$).

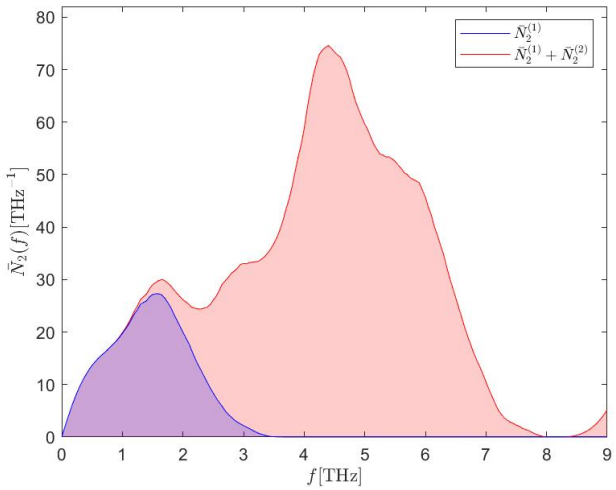

Fig. S40 Averaged two-phonon weighted joint density of states (w-JDoS) functions $\bar{N}_2(f)$ for $Fm\bar{3}m$ SnTe at $T = 300$ K. The plot is drawn as a stacked area plot showing the contributions from collision ($\bar{N}_2^{(1)}$) and decay ($\bar{N}_2^{(2)}$) processes in blue and red, respectively (the red line shows the sum $\bar{N}_2^{(1)} + \bar{N}_2^{(2)}$).

5 Three-phonon interaction strengths

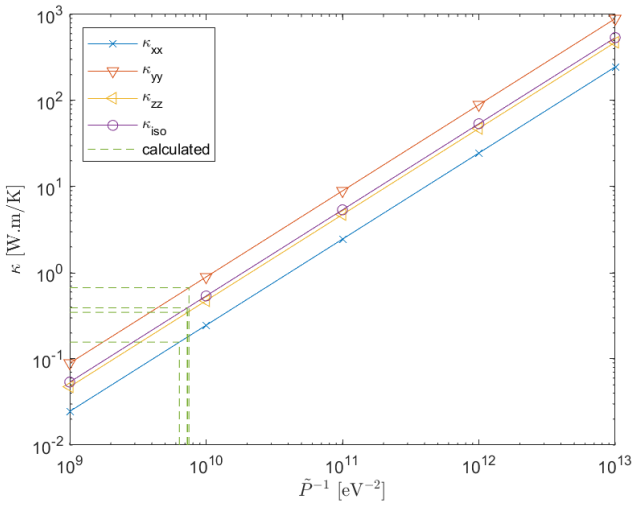

Fig. S41 Determination of the averaged three-phonon interaction strength $\tilde{P}$ at $T = 300$ K for *Pnma* GeSe from a linear fit of the $\boldsymbol{\kappa}_{\text{latt}}$ as a function of $\tilde{P}^{-1}$.

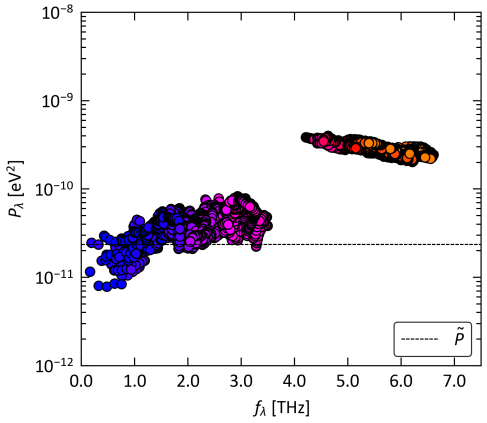

Fig. S42 Comparison of the averaged three-phonon interaction strength $\tilde{P}$ at $T = 300$ K for *Pnma* GeSe to the spectrum of the averaged modal three-phonon interaction strengths P_λ.

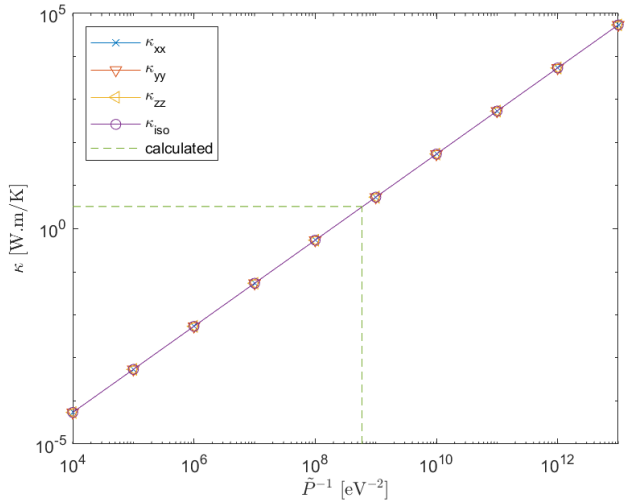

Fig. S43 Determination of the averaged three-phonon interaction strength $\tilde{P}$ at $T = 300$ K for $Fm\bar{3}m$ GeSe from a linear fit of the $\boldsymbol{\kappa}_{\text{latt}}$ as a function of $\tilde{P}^{-1}$.

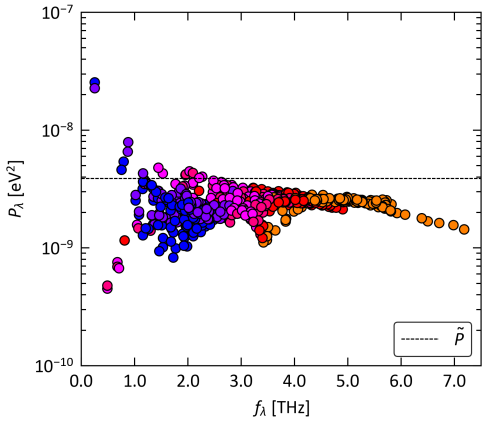

Fig. S44 Comparison of the averaged three-phonon interaction strength $\tilde{P}$ at $T = 300$ K for $Fm\bar{3}m$ GeSe to the spectrum of the averaged modal three-phonon interaction strengths P_λ.

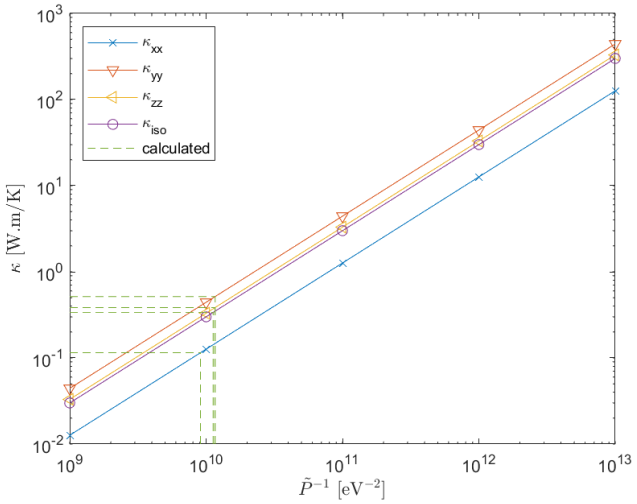

Fig. S45 Determination of the averaged three-phonon interaction strength $\tilde{P}$ at $T = 300$ K for *Pnma* GeTe from a linear fit of the $\boldsymbol{\kappa}_{\text{latt}}$ as a function of $\tilde{P}^{-1}$.

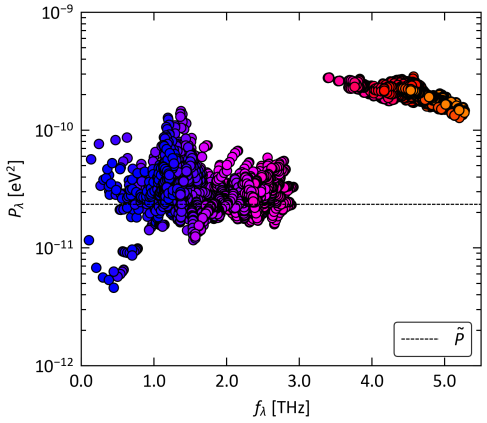

Fig. S46 Comparison of the averaged three-phonon interaction strength $\tilde{P}$ at $T = 300$ K for *Pnma* GeTe to the spectrum of the averaged modal three-phonon interaction strengths P_λ.

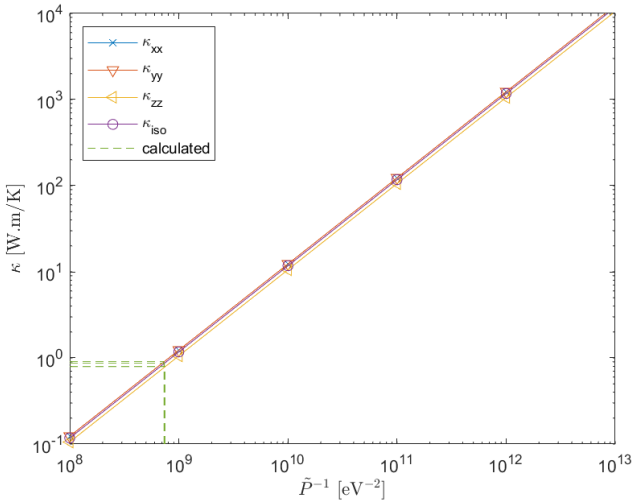

Fig. S47 Determination of the averaged three-phonon interaction strength $\tilde{P}$ at $T = 300$ K for $R3m$ GeTe from a linear fit of the $\boldsymbol{\kappa}_{\mathrm{latt}}$ as a function of $\tilde{P}^{-1}$.

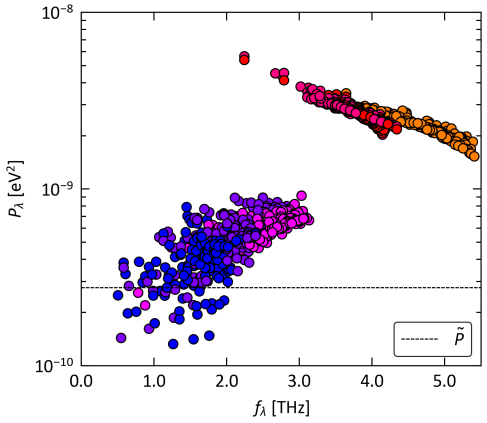

Fig. S48 Comparison of the averaged three-phonon interaction strength $\tilde{P}$ at $T = 300$ K for $R3m$ GeTe to the spectrum of the averaged modal three-phonon interaction strengths P_λ.

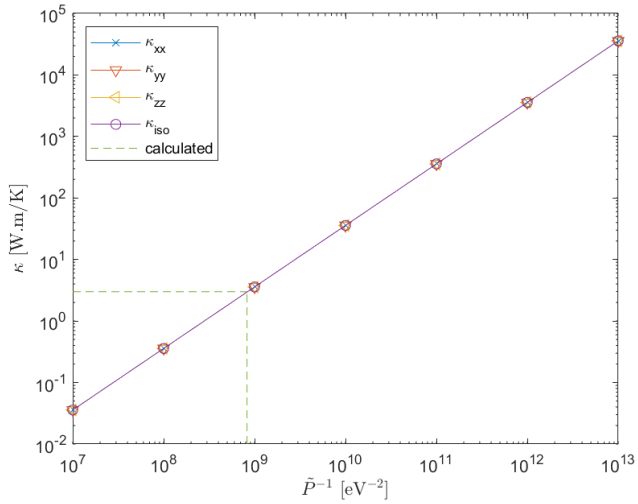

Fig. S49 Determination of the averaged three-phonon interaction strength $\tilde{P}$ at $T = 300$ K for $Fm\bar{3}m$ GeTe from a linear fit of the $\boldsymbol{\kappa}_{\text{latt}}$ as a function of $\tilde{P}^{-1}$.

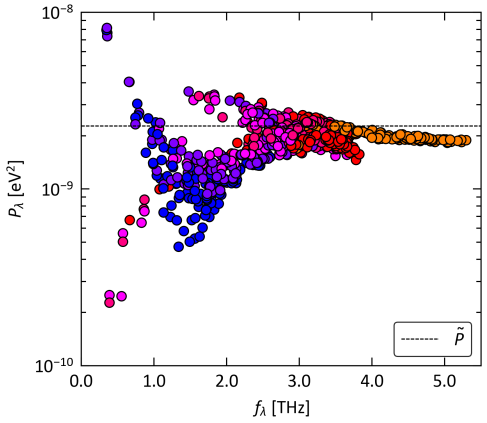

Fig. S50 Comparison of the averaged three-phonon interaction strength $\tilde{P}$ at $T = 300$ K for $Fm\bar{3}m$ GeTe to the spectrum of the averaged modal three-phonon interaction strengths P_λ.

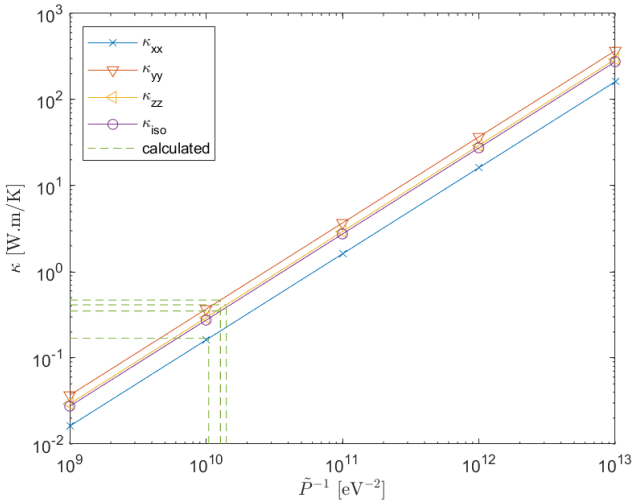

Fig. S51 Determination of the averaged three-phonon interaction strength $\tilde{P}$ at $T = 300$ K for *Pnma* SnSe from a linear fit of the $\boldsymbol{\kappa}_{\text{latt}}$ as a function of $\tilde{P}^{-1}$.

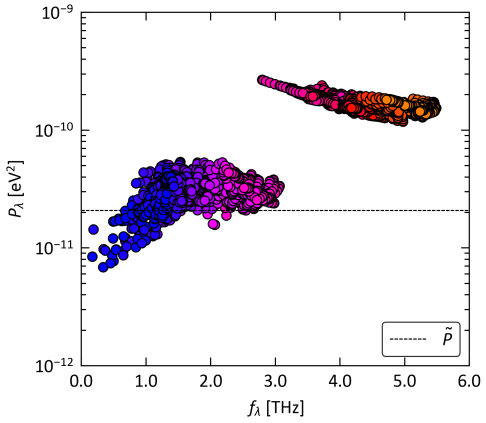

Fig. S52 Comparison of the averaged three-phonon interaction strength $\tilde{P}$ at $T = 300$ K for *Pnma* SnSe to the spectrum of the averaged modal three-phonon interaction strengths P_λ.

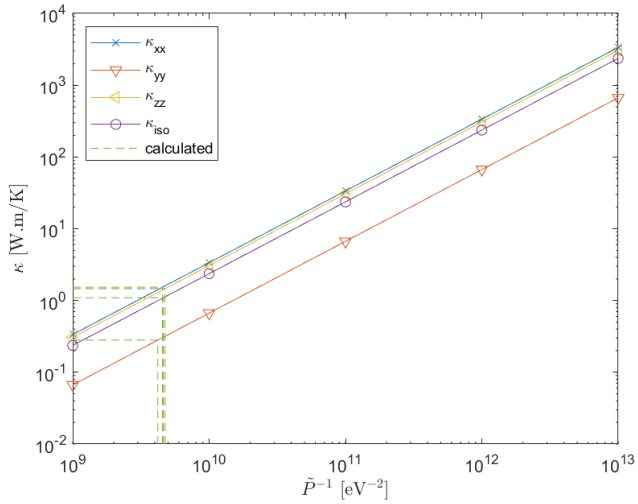

Fig. S53 Determination of the averaged three-phonon interaction strength $\tilde{P}$ at $T = 300$ K for *Cmcm* SnSe from a linear fit of the $\boldsymbol{\kappa}_{\text{latt}}$ as a function of $\tilde{P}^{-1}$.

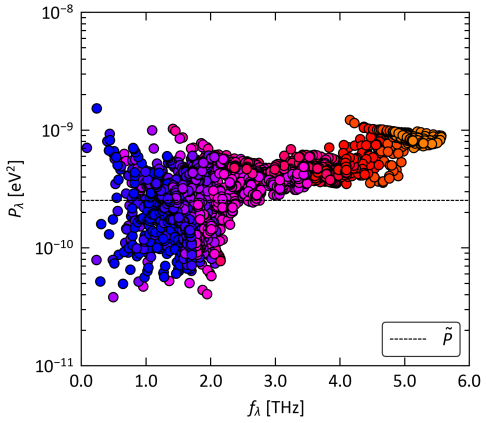

Fig. S54 Comparison of the averaged three-phonon interaction strength $\tilde{P}$ at $T = 300$ K for *Cmcm* SnSe to the spectrum of the averaged modal three-phonon interaction strengths P_λ.

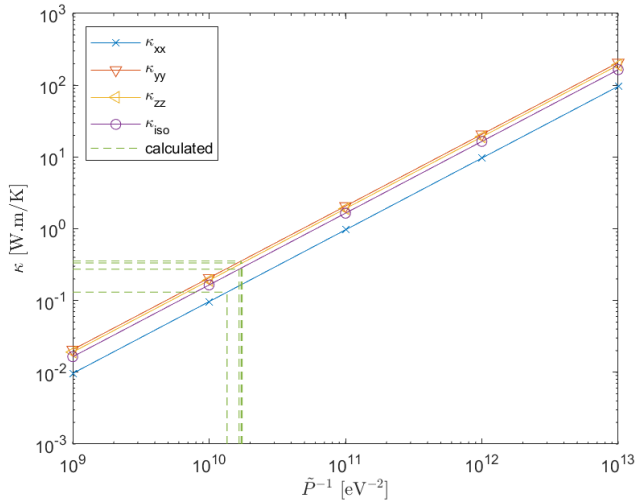

Fig. S55 Determination of the averaged three-phonon interaction strength $\tilde{P}$ at $T = 300$ K for *Pnma* SnTe from a linear fit of the $\boldsymbol{\kappa}_{\mathrm{latt}}$ as a function of $\tilde{P}^{-1}$.

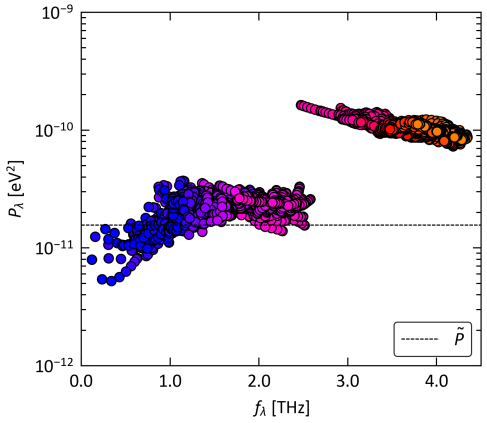

Fig. S56 Comparison of the averaged three-phonon interaction strength $\tilde{P}$ at $T = 300$ K for *Pnma* SnTe to the spectrum of the averaged modal three-phonon interaction strengths P_λ.

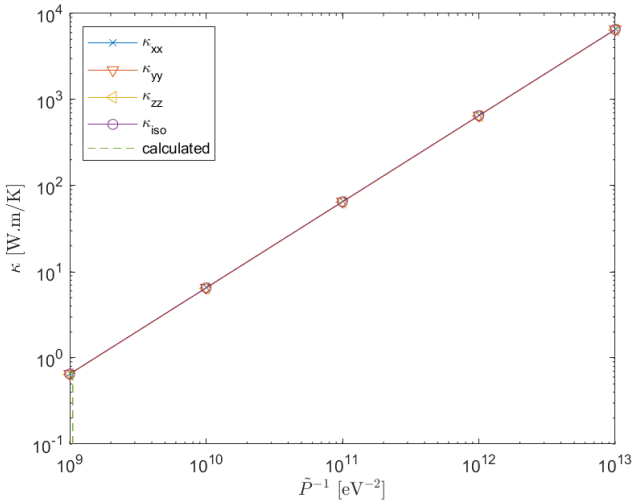

Fig. S57 Determination of the averaged three-phonon interaction strength $\tilde{P}$ at $T = 300$ K for $R3m$ SnTe from a linear fit of the $\boldsymbol{\kappa}_{\text{latt}}$ as a function of $\tilde{P}^{-1}$.

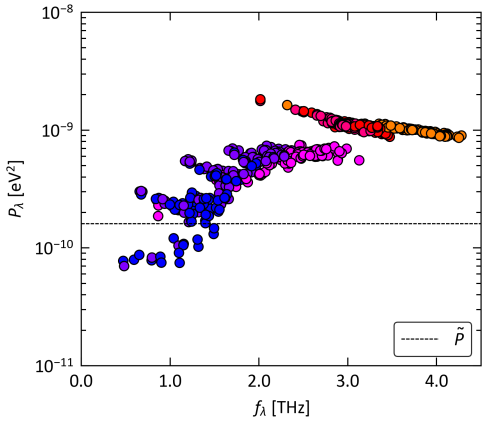

Fig. S58 Comparison of the averaged three-phonon interaction strength $\tilde{P}$ at $T = 300$ K for $R3m$ SnTe to the spectrum of the averaged modal three-phonon interaction strengths P_λ.

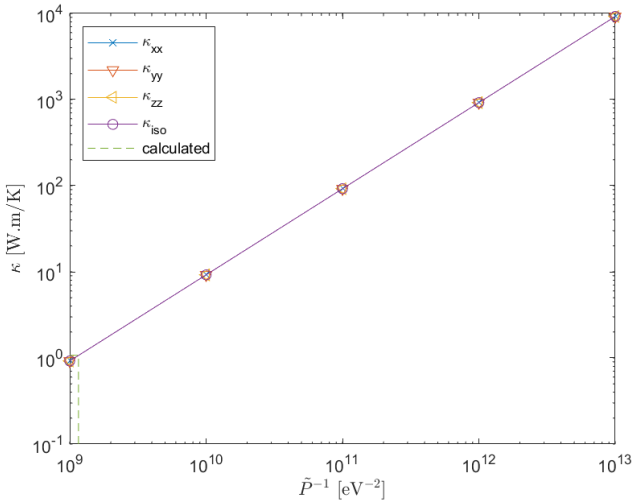

Fig. S59 Determination of the averaged three-phonon interaction strength $\tilde{P}$ at $T = 300$ K for $Fm\bar{3}m$ SnTe from a linear fit of the $\boldsymbol{\kappa}_{\text{latt}}$ as a function of $\tilde{P}^{-1}$.

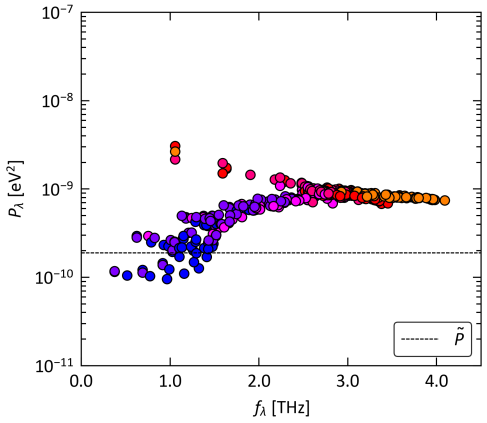

Fig. S60 Comparison of the averaged three-phonon interaction strength $\tilde{P}$ at $T = 300$ K for $Fm\bar{3}m$ SnTe to the spectrum of the averaged modal three-phonon interaction strengths P_λ.

6 Relaxation-time approximation and linearised Boltzmann transport equation

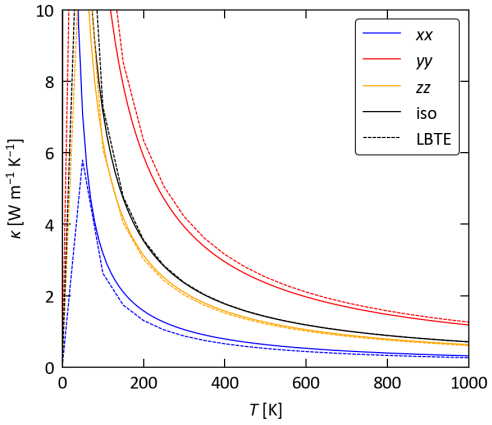

Fig. S61 Comparison of the lattice thermal conductivity of *Pnma* GeSe calculated within the relaxation-time approximation (RTA; solid lines) and by direct solution of the linearised Boltzmann transport equation (LBTE; dashed lines). The diagonal κ_{xx}, κ_{yy} and κ_{zz} of the $\boldsymbol{\kappa}_{\mathrm{latt}}$ tensors are shown together with the average $\kappa_{\mathrm{iso}} = (\kappa_{xx} + \kappa_{yy} + \kappa_{zz})/3$.

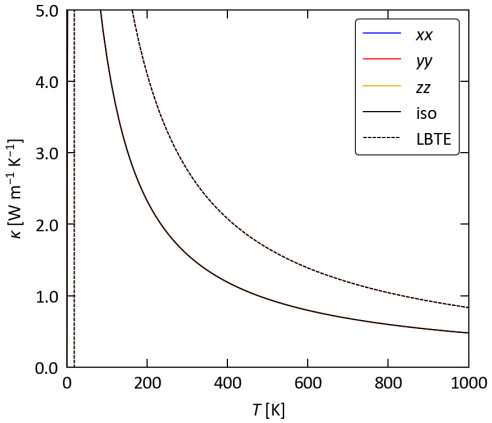

Fig. S62 Comparison of the lattice thermal conductivity of $Fm\bar{3}m$ GeSe calculated within the relaxation-time approximation (RTA; solid lines) and by direct solution of the linearised Boltzmann transport equation (LBTE; dashed lines). The diagonal κ_{xx}, κ_{yy} and κ_{zz} of the $\boldsymbol{\kappa}_{\mathrm{latt}}$ tensors are shown together with the average $\kappa_{\mathrm{iso}} = (\kappa_{xx} + \kappa_{yy} + \kappa_{zz})/3$.

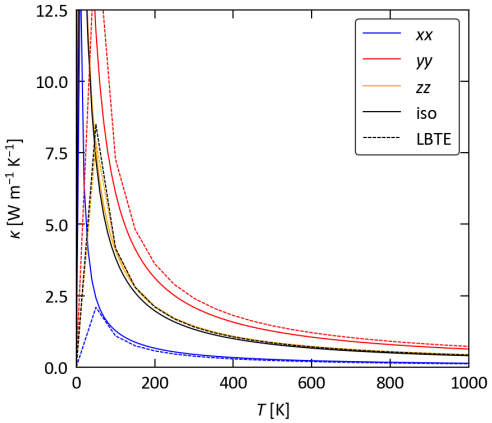

Fig. S63 Comparison of the lattice thermal conductivity of *Pnma* GeTe calculated within the relaxation-time approximation (RTA; solid lines) and by direct solution of the linearised Boltzmann transport equation (LBTE; dashed lines). The diagonal κ_{xx}, κ_{yy} and κ_{zz} of the $\boldsymbol{\kappa}_{\mathrm{latt}}$ tensors are shown together with the average $\kappa_{\mathrm{iso}} = (\kappa_{xx} + \kappa_{yy} + \kappa_{zz})/3$.

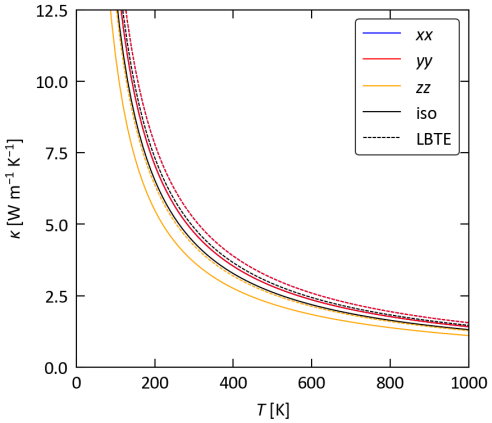

Fig. S64 Comparison of the lattice thermal conductivity of *R3m* GeTe calculated within the relaxation-time approximation (RTA; solid lines) and by direct solution of the linearised Boltzmann transport equation (LBTE; dashed lines). The diagonal κ_{xx}, κ_{yy} and κ_{zz} of the $\boldsymbol{\kappa}_{\mathrm{latt}}$ tensors are shown together with the average $\kappa_{\mathrm{iso}} = (\kappa_{xx} + \kappa_{yy} + \kappa_{zz})/3$.

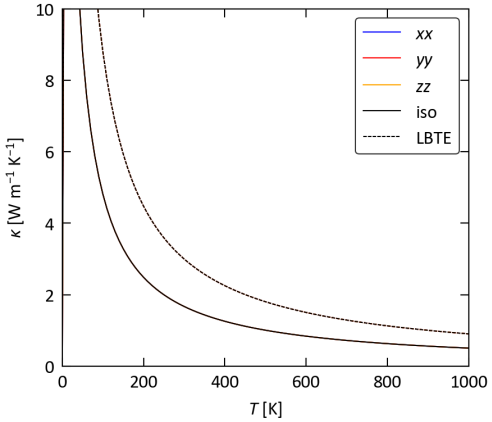

Fig. S65 Comparison of the lattice thermal conductivity of $Fm\bar{3}m$ GeTe calculated within the relaxation-time approximation (RTA; solid lines) and by direct solution of the linearised Boltzmann transport equation (LBTE; dashed lines). The diagonal κ_{xx}, κ_{yy} and κ_{zz} of the $\boldsymbol{\kappa}_{\mathrm{latt}}$ tensors are shown together with the average $\kappa_{\mathrm{iso}} = (\kappa_{xx} + \kappa_{yy} + \kappa_{zz})/3$.

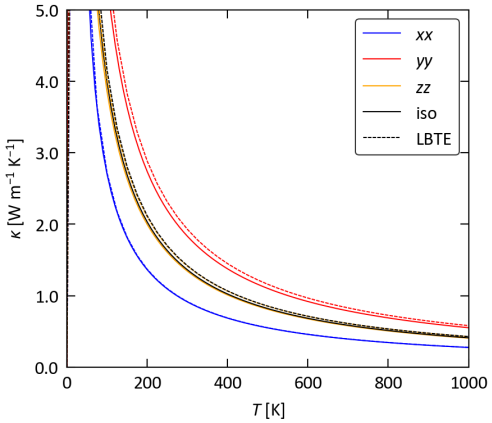

Fig. S66 Comparison of the lattice thermal conductivity of *Pnma* SnSe calculated within the relaxation-time approximation (RTA; solid lines) and by direct solution of the linearised Boltzmann transport equation (LBTE; dashed lines). The diagonal κ_{xx}, κ_{yy} and κ_{zz} of the $\boldsymbol{\kappa}_{\mathrm{latt}}$ tensors are shown together with the average $\kappa_{\mathrm{iso}} = (\kappa_{xx} + \kappa_{yy} + \kappa_{zz})/3$.

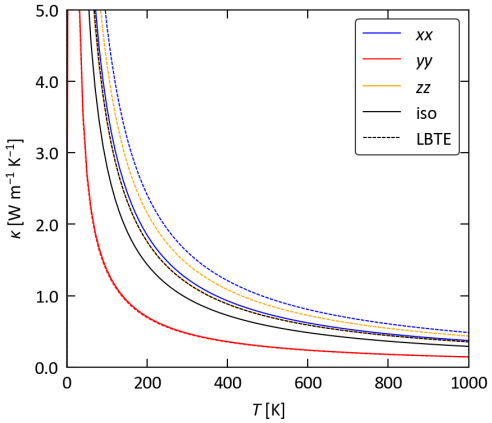

Fig. S67 Comparison of the lattice thermal conductivity of *Cmcm* SnSe calculated within the relaxation-time approximation (RTA; solid lines) and by direct solution of the linearised Boltzmann transport equation (LBTE; dashed lines). The diagonal κ_{xx}, κ_{yy} and κ_{zz} of the $\boldsymbol{\kappa}_{\mathrm{latt}}$ tensors are shown together with the average $\kappa_{\mathrm{iso}} = (\kappa_{xx} + \kappa_{yy} + \kappa_{zz})/3$.

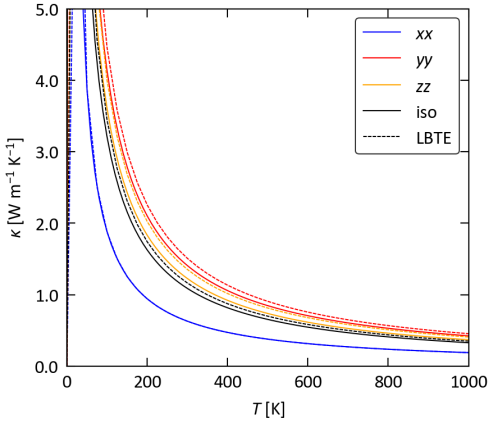

Fig. S68 Comparison of the lattice thermal conductivity of *Pnma* SnTe calculated within the relaxation-time approximation (RTA; solid lines) and by direct solution of the linearised Boltzmann transport equation (LBTE; dashed lines). The diagonal κ_{xx}, κ_{yy} and κ_{zz} of the $\boldsymbol{\kappa}_{\mathrm{latt}}$ tensors are shown together with the average $\kappa_{\mathrm{iso}} = (\kappa_{xx} + \kappa_{yy} + \kappa_{zz})/3$.

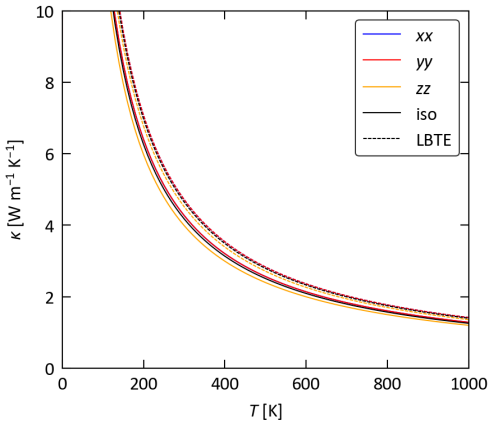

Fig. S69 Comparison of the lattice thermal conductivity of $R3m$ SnTe calculated within the relaxation-time approximation (RTA; solid lines) and by direct solution of the linearised Boltzmann transport equation (LBTE; dashed lines). The diagonal κ_{xx}, κ_{yy} and κ_{zz} of the $\boldsymbol{\kappa}_{\mathrm{latt}}$ tensors are shown together with the average $\kappa_{\mathrm{iso}} = (\kappa_{xx} + \kappa_{yy} + \kappa_{zz})/3$.

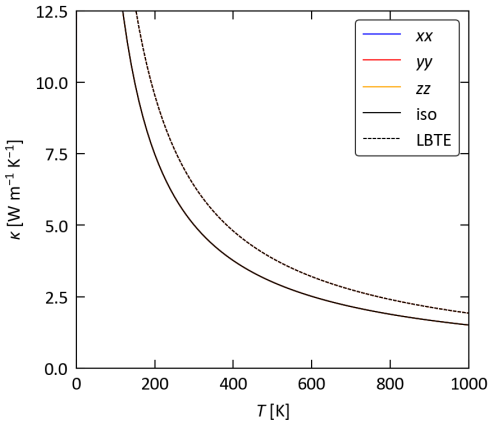

Fig. S70 Comparison of the lattice thermal conductivity of $Fm\bar{3}m$ SnTe calculated within the relaxation-time approximation (RTA; solid lines) and by direct solution of the linearised Boltzmann transport equation (LBTE; dashed lines). The diagonal κ_{xx}, κ_{yy} and κ_{zz} of the $\boldsymbol{\kappa}_{\mathrm{latt}}$ tensors are shown together with the average $\kappa_{\mathrm{iso}} = (\kappa_{xx} + \kappa_{yy} + \kappa_{zz})/3$.

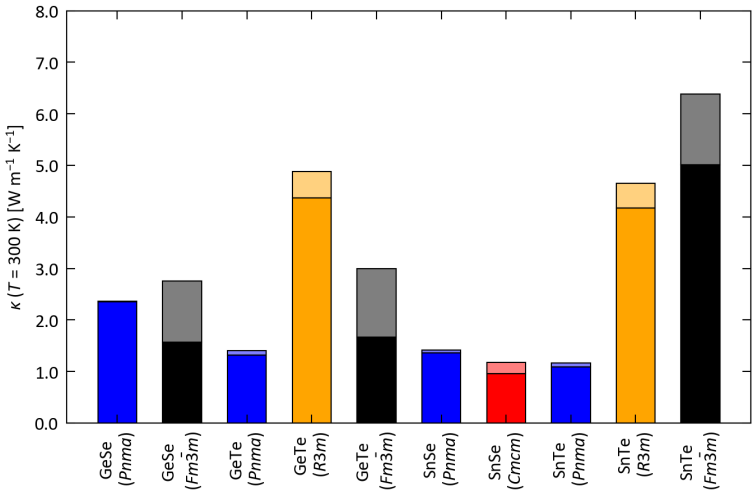

Fig. S71 Comparison of the averaged lattice thermal conductivity $\kappa_{\mathrm{iso}} = (\kappa_{xx} + \kappa_{yy} + \kappa_{zz})/3$ of the ten systems examined in this work at $T = 300$ K calculated within the relaxation-time approximation (RTA; solid bars) and by direct solution of the linearised Boltzmann transport equation (LBTE; shaded bars).

7 Ioffe-Regel limit in time

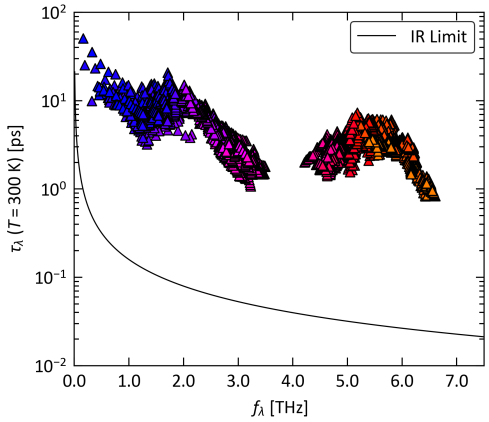

Fig. S72 Comparison of the spectrum of phonon lifetimes for *Pnma* GeSe at $T = 300$ K to the Ioffe-Regel limit of $1/(2\pi\nu)$.

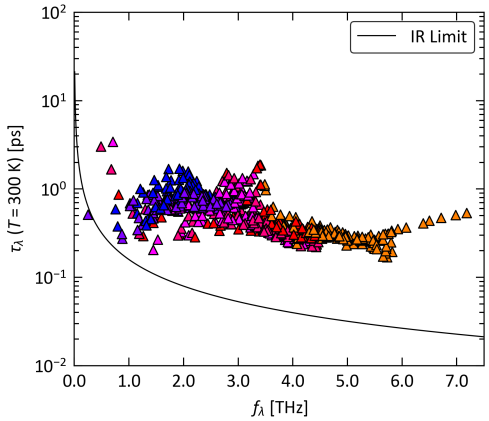

Fig. S73 Comparison of the spectrum of phonon lifetimes for $Fm\bar{3}m$ GeSe at $T = 300$ K to the Ioffe-Regel limit of $1/(2\pi\nu)$.

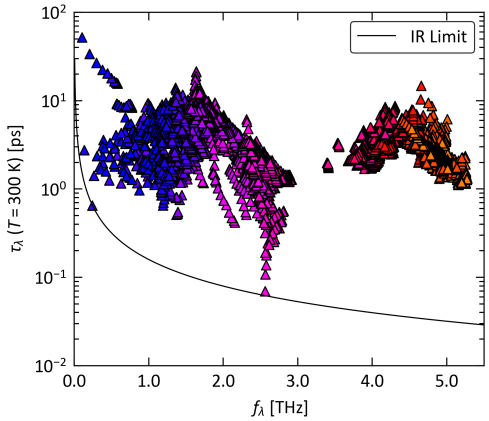

Fig. S74 Comparison of the spectrum of phonon lifetimes for $Pnma$ GeTe at $T = 300$ K to the Ioffe-Regel limit of $1/(2\pi\nu)$.

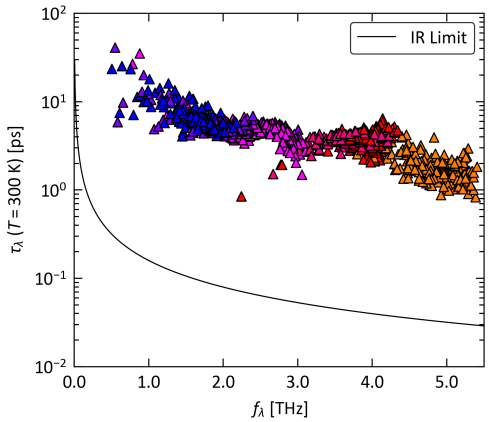

Fig. S75 Comparison of the spectrum of phonon lifetimes for $R3m$ GeTe at $T = 300$ K to the Ioffe-Regel limit of $1/(2\pi\nu)$.

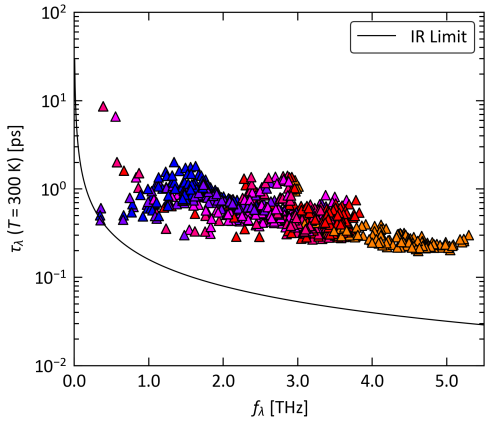

Fig. S76 Comparison of the spectrum of phonon lifetimes for $Fm\bar{3}m$ GeTe at $T = 300$ K to the Ioffe-Regel limit of $1/(2\pi\nu)$.

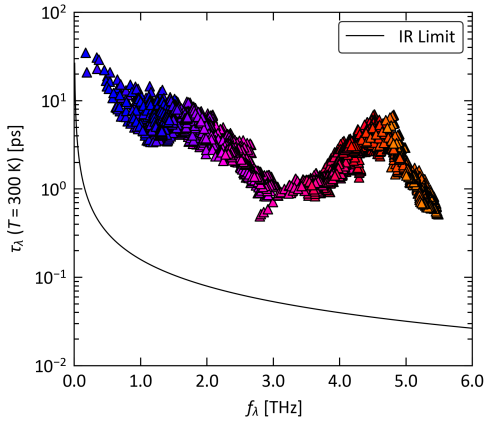

Fig. S77 Comparison of the spectrum of phonon lifetimes for *Pnma* SnSe at $T = 300$ K to the Ioffe-Regel limit of $1/(2\pi\nu)$.

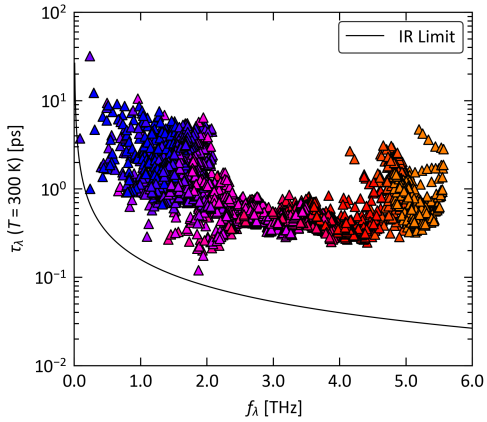

Fig. S78 Comparison of the spectrum of phonon lifetimes for *Cmcm* SnSe at $T = 300$ K to the Ioffe-Regel limit of $1/(2\pi\nu)$.

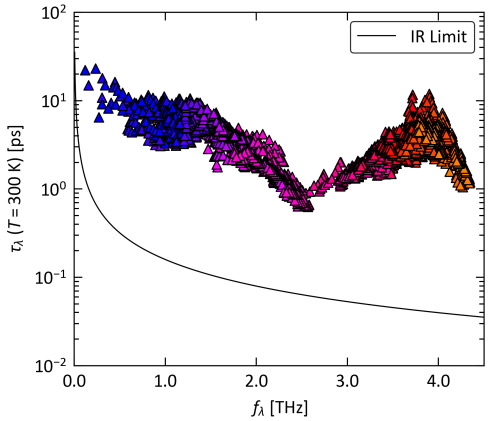

Fig. S79 Comparison of the spectrum of phonon lifetimes for *Pnma* SnTe at $T = 300$ K to the Ioffe-Regel limit of $1/(2\pi\nu)$.

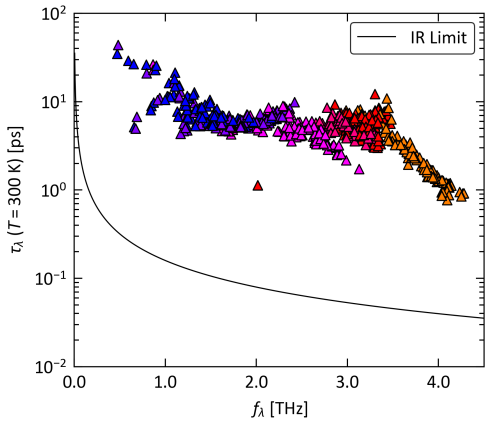

Fig. S80 Comparison of the spectrum of phonon lifetimes for $R3m$ SnTe at $T = 300$ K to the Ioffe-Regel limit of $1/(2\pi\nu)$.

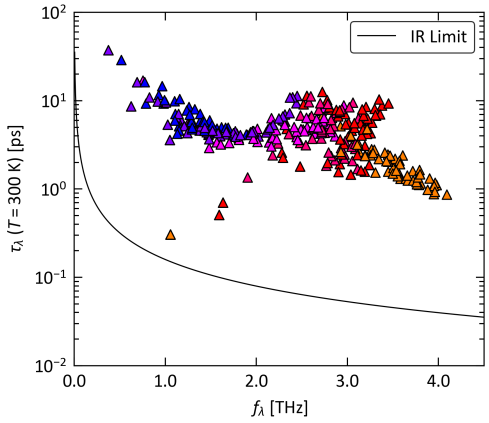

Fig. S81 Comparison of the spectrum of phonon lifetimes for $Fm\bar{3}m$ SnTe at $T = 300$ K to the Ioffe-Regel limit of $1/(2\pi\nu)$.